

Locking the Kink in the Influenza Hemagglutinin Fusion Domain Structure^{*S}

Received for publication, May 15, 2007, and in revised form, June 8, 2007. Published, JBC Papers in Press, June 12, 2007, DOI 10.1074/jbc.M704008200

Alex L. Lai and Lukas K. Tamm¹

From the Department of Molecular Physiology and Biological Physics, University of Virginia, Charlottesville, Virginia 22908

We have previously identified Trp¹⁴ as a critical residue that stabilizes the kink in the boomerang structure of the influenza fusion domain and found that cells expressing hemagglutinin with a Trp¹⁴ to Ala mutation cannot fuse with red blood cells. However, mutating another aromatic residue, Phe⁹, on the other side of the kink did not have a significant effect on fusion or the ability of the mutant fusion peptide to bind to or perturb the bilayer structure of lipid model membranes. We reasoned that Phe is not as potent to contribute to the kink as the larger Trp and that the cooperation of Phe⁹ and Ile¹⁰ might be needed to elicit the same effect. Indeed, the double mutant F9A/I10A diminished cell-cell fusion and the ability of the fusion domain to bind to and perturb lipid bilayers in a similar fashion as the W14A mutant. A structure determination of F9A in lipid micelles by solution NMR shows that F9A adopts a similarly kinked structure as wild type. Distances between the two arms of the boomerang structure of wild type, F9A, W14A, and F9A/I10A in lipid bilayers were measured by double electron-electron resonance spectroscopy and showed that the kinks of W14A and F9A/I10A are more flexible than those of wild type and F9A. These results underscore the importance of large hydrophobic residues on both sides of the kink region of the influenza hemagglutinin fusion domain to fix the angle of the boomerang structure and thereby confer fusion function to this critical domain.

Enveloped viruses enter host cells by membrane fusion. Influenza virus, as an example, first attaches to the plasma membrane of the host cell, and the virus is then taken up by the host cell by receptor-mediated endocytosis. When the pH in the endosome decreases to around 5, influenza hemagglutinin (HA)² on the viral envelope undergoes a dramatic conforma-

tional change, which triggers fusion of the viral and endosome membranes. Each monomer of the HA homotrimer consists of two subunits, HA1 and HA2. While HA1 is responsible for receptor recognition, HA2, which also anchors HA in the viral membrane, is responsible for membrane fusion. The fusion domain or fusion peptide of HA consists of a relatively hydrophobic sequence located at the N terminus of the HA2 subunit. Under resting condition at neutral pH, the fusion domains are buried in hydrophobic pockets at the interfaces between monomers in the HA trimer. However, under acidic conditions, the fusion domains become exposed and insert into the endosomal target membrane of the host cell, where they initiate fusion. A single fusion site is thought to consist of several HA trimers. Thus, multiple fusion domains are suggested to work cooperatively to merge the two membranes. In addition to these fusion domain-lipid interactions, the pH-induced conformational change also tilts the coiled-coil rods of HA2 relative to the two membranes and thereby drags them into close proximity (1). Some current models of HA-mediated membrane fusion suggest that there are interactions between the transmembrane and fusion domains and that these interactions may facilitate late steps of membrane fusion (2).

The fusion domain of influenza HA consists of ~24 quite highly conserved residues, of which six are glycines. The sequence is overall quite hydrophobic, but also contains a few polar residues. The structure of the HA fusion domain has been determined by solution NMR spectroscopy in DPC micelles and its disposition and depth of membrane penetration has been determined by site-directed spin-label EPR spectroscopy in lipid bilayers (3). At pH 5, the domain adopts a shallow angle boomerang structure, with an α -helix in the N-terminal arm and a short 3_{10} -helix in the C-terminal arm. The domain docks into lipid bilayers with the N-terminal and C-terminal arms inserting into the hydrophobic core of the bilayer, while the apex of the kink, Asn¹², is located in the hydrophilic head group region of the bilayer. The structure and lipid interaction of the non-fusogenic mutant, W14A, is very different and its location in the bilayer also differs significantly from that of the wild-type structure (4). The N-terminal arm lies almost parallel in the interface and the C-terminal arm is very flexible and points out

* This work was supported by Grant R37 AI30557 from the NIAID, National Institutes of Health. The costs of publication of this article were defrayed in part by the payment of page charges. This article must therefore be hereby marked "advertisement" in accordance with 18 U.S.C. Section 1734 solely to indicate this fact.

The atomic coordinates and structure factors (code 2JRD) have been deposited in the Protein Data Bank, Research Collaboratory for Structural Bioinformatics, Rutgers University, New Brunswick, NJ (<http://www.rcsb.org/>).

^S The on-line version of this article (available at <http://www.jbc.org>) contains supplemental Tables S1 and S2 and Figs. S1–S4.

¹ To whom correspondence should be addressed. Tel.: 434-982-3578; Fax: 434-982-1616; E-mail: lkt2e@virginia.edu.

² The abbreviations used are: HA, hemagglutinin; ATR, attenuated total reflection; CD, circular dichroism; CF, carboxyfluorescein; CW, continuous wave; DPC, dodecylphosphocholine; DEER, double electron-electron resonance; EPR, electron paramagnetic resonance; FACS, fluorescence-activated cell sorter; FTIR, Fourier transform infrared; LUV, large unilamellar vesicle; MES,

4-morpholineethanesulfonic acid; MTSSL, (1-oxyl-2,2,5,5-tetramethyl-3-pyrroline-3-methyl) methanethiosulfonate spin label; NiEDDA, nickel(II)-ethylenediamine-*N,N'*-diacetic acid; NMR, nuclear magnetic resonance; NOESY, nuclear Overhauser effect spectroscopy; POPC, 1-palmitoyl-2-oleoyl-*sn*-glycero-3-phosphocholine; POPG, 1-palmitoyl-2-oleoyl-*sn*-glycero-3-phosphoglycerol; R18, octadecyl-rhodamine B; RBC, red blood cell; r.m.s.d., root mean square deviation; SUV, small unilamellar vesicle; TOCSY, total correlation spectroscopy; WT, wild-type.

of the membrane without adopting a regular secondary structure. W14A also binds more weakly to model membranes and perturbs the order of lipid bilayers to lesser degree than the wild-type fusion domain. These results suggested that a boomerang structure with a fixed kink angle is important to confer fusion activity to HA. Because Phe⁹ is on the opposite side of the kink region but still close to the other aromatic residue, Trp¹⁴, in the wild-type structure and since a hydrogen bond between the amide NH of Trp¹⁴ and the carbonyl of Phe⁹ has been thought to stabilize the kink region, we initially hypothesized that Phe⁹ and Trp¹⁴ might serve similar functions in stabilizing the kink region (3). However, later studies showed that the F9A mutation supports full fusion in cell-cell fusion assays, and its strength of membrane binding and lipid perturbation is also similar to that of the wild type (4). Therefore, the Phe⁹ and Trp¹⁴ are not the only residues that contribute to the stability of the kink region. Additional residues may contribute to the hydrophobic pocket in this region, stabilizing the angled structure and thereby supporting the function of the fusion domain. To examine this hypothesis, we made additional mutations of hydrophobic residues in the kink region of full-length HA and studied their effect on membrane fusion. We also used peptide models of the same mutations to assess their effects on lipid interactions that could explain their altered fusion activities. To establish that a fixed-angle boomerang structure is indeed necessary to promote fusion, we solved the structure of the F9A mutant fusion domain and measured the flexibility of the kink of wild-type and several mutant fusion domains in lipid bilayers.

EXPERIMENTAL PROCEDURES

Peptides and Lipids—All peptides were synthesized by the Biomolecular Research Facility at the University of Virginia. Lipids and detergents were purchased from Avanti Polar Lipids (Alabaster, AL).

Mutagenesis and HA Expression—Mutations were introduced into the pTM-HA (X:31) vector using the QuikChange site-directed mutagenesis kit (Stratagene). Primers were from Integrated DNA Technologies. The sequence of F9A/I10A was confirmed by complete sequencing. All other mutants were sequenced in the region around the fusion domains (> 500 bp). Wild-type and mutant HAs were expressed in CV-1 cells as described previously using 1 μ g of DNA for each transfection (4). Immunoprecipitation and FACS were carried out as previously described (5). SDS-gels were developed with streptavidin-horseradish peroxidase.

Fusion Assays—Fusion between HA-expressing CV-1 cells that were treated with neuraminidase and trypsin and fresh human red blood cells that were double-labeled with octadecylrhodamine B chloride and carboxyfluorescein (both from Molecular Probes) was measured after a 5-min exposure to pH 5 on a Zeiss Axiovert 200 fluorescence microscope (4). The lipid and contents mixing ratios are defined as the ratios of the number of CV-1 cells that undergo lipid or content mixing to the number of CV-1 cells that bound RBCs. Bulk fluorescence dequenching experiments were carried out in a Jobin-Yvon Fluorolog 3 spectrofluorometer (4). Percent fluorescence dequenching was calculated as $(F_1 - F_0)/(F_{\text{det}} - F_0) \times 100$,

where F_1 is the fluorescence intensity at the end of the pH 5 incubation period and before the addition of detergent, F_0 is the fluorescence during the initial pH 7.0 incubation, and F_{det} is the fluorescence during the final incubation in the presence of 1% Triton X-100.

Preparation of Liposomes—Desired amounts of POPC and POPG were mixed in chloroform and dried overnight under vacuum. Fusion buffer (5 mM HEPES, 10 mM MES, pH 5) was added and vortexed to give 5 mM lipid dispersions. To prepare SUVs, the dispersion was sonicated in an ice-water bath using a Branson titanium tip ultrasonicator for ~1 h at 50% duty cycle until it was transparent. To prepare LUVs, the dispersion was five times frozen and thawed in liquid nitrogen and a 37 °C water bath, followed by extrusion (15 times) through polycarbonate membranes with 100-nm pores (Avestin, Ottawa, CN).

Isothermal Titration Calorimetry—All measurements were carried out at 25 °C in a high-sensitivity MCS titration calorimeter (MicroCal Inc). For reaction enthalpy measurements, 10- μ l aliquots of peptide at a concentration of around 18 μ M were injected into the sample cell containing 2 ml of 5 mM POPC:POPG (4:1) SUVs. For free energy measurements, 10- μ l aliquots of 5 mM POPC:POPG (4:1) SUVs were injected into the sample cell containing 2 ml of 1 mM peptide. Exact concentrations of peptides were determined by quantitative amino acid analysis. The data were analyzed as previously described (4).

Circular Dichroism and Fourier Transform Infrared Spectroscopy—CD spectra of fusion domains bound to SUVs, LUVs, or DPC micelles were measured at peptide:lipid ratios of 1:200 at 25 °C in an model 215 spectropolarimeter (AVIV). Polarized ATR-FTIR spectra of fusion domains bound to supported bilayers on germanium ATR plates were recorded on a Vector 22 FTIR spectrometer (Bruker) and analyzed as described (4, 6).

NMR Spectroscopy and Structure Calculation—The sample was prepared by mixing the 2 mM F9A fusion domain and 200 mM DPC in pH 5 buffer. All NMR spectra were collected on a Inova 600 MHz NMR spectrometer (Varian). The data were processed with the program NMRPipe (7), and the resonance assignments were completed with the program Sparky (T. D. Goddard and D. G. Kneller, University of California, San Francisco). Structural ensembles were calculated using the program DYANA (8). The 30 conformers with the lowest energy target function value were further energy-minimized using the program OPAL with the Amber94 force field (8). The energy-minimized conformers were aligned and displayed using the program MOLMOL (9).

Continuous Wave EPR Spectroscopy—Fusion domains were labeled with the spin-label MTSSL and purified as previously described (3). Labeling was monitored by mass spectrometry. For line-shape analysis and distance measurements, samples were mixed with molar ratios of 1:500 DPC, 1:200 SUV, or 1:200 LUV in pH 5 buffer and incubated for at least 20 min. The samples were then sealed in glass capillary tubes with an inner diameter of 0.60 mm (VitroCom Inc). To ensure the removal of potential free spin-labels, some samples were first diluted 10 times and then concentrated through a Microcon centrifugal filter with a cutoff size of 3 kDa (Millipore, Bedford, MA). EPR spectra were recorded on an E-line Centuries Series spectrom-

Influenza HA Fusion Domain

eter (Varian). All spectra for line-shape analysis and CW distance determinations were recorded at 2.0 milliwatt incident power at room temperature. For power saturation measurements, the spin-labeled fusion domains were mixed with POPC:POPG (4:1) LUVs at a molar ratio of 1:1000. Spectra were collected in the presence of nitrogen, air, and nitrogen with 20 mM NiEDDA, respectively, as described previously (3). All spectra were analyzed with the Labview EPR analysis software developed by Drs. C. Altenbach and W. Hubbell.

Double Electron-Electron Resonance Spectroscopy—The samples contained 100 μM double-spin-labeled fusion domains bound to POPC:POPG(4:1) LUVs at molar a ratio of 1:200 in pH 5 buffer. DEER measurements were performed at a temperature of 80 K on a EleXSys 580 spectrometer (Bruker) equipped with a 2 mm split-ring resonator. The samples were flash-frozen in liquid nitrogen immediately before insertion into the resonator. The four-pulse sequence $(\pi/2)_{\nu_1} - \tau_1 - (\pi)_{\nu_1} - t - (\pi)_{\nu_2} - (\tau_1 + \tau_2 - t) - (\pi)_{\nu_1} - \tau_2$ -echo was used (ν_1 , observe frequency; ν_2 , pump frequency; π_{ν_1} , 32-ns pulse; π_{ν_2} , 32-ns pump pulse; τ_1 , 200-ns delay; τ_2 , 1200-ns delay; t , dipolar evolution time) (10). The observed and pump frequencies were selected from the positions of the center and low field EPR maxima, respectively, of the CW spectra of each sample. 70 or more scans were added for each spectrum. Data were analyzed with the program DEERAnalysis 2006 developed by Dr. G. Jeschke. A homogeneous two-dimensional background model was applied to fit the data.

Docking of NMR Structure to EPR Depth Data—The NMR structural conformer with the smallest r.m.s.d. to the mean structure of the 35 conformers was substituted with spin labels in the four measured positions. This structure was docked with the program Insight II (Accelrys) to a lipid bilayer using the depth data obtained from the EPR power saturation experiments. The dihedral angles χ_1 and χ_2 were set to 300°. The values of χ_3 were determined for each site by energy minimization with the Amber force field and restricting their values to either +90 (p) or -90 (n). The energy-minimized structure of the substituted F9A fusion domain had the χ_3 combination pnpn for the four consecutively labeled residues.

RESULTS

Fusion Activity of HA Mutants—The influenza HA fusion domain adopts a boomerang structure in membranes at pH 5 with two helical arms on either side of the kink at Asn¹². Because the two aromatic residues Phe⁹ and Trp¹⁴ that face each other on opposite sides of the kink have different effects on fusion, we reasoned that the smaller Phe⁹ needs the help of the neighboring Ile¹⁰ to elicit the same effect on fusion as Trp¹⁴. To test this hypothesis, we made two new mutants in the kink region, the single-site mutant I10A and the double-site mutant F9A/I10A, examined their effects on fusion, and compared them to the previously described mutants F9A and W14A (4).

Fusion was first examined by fluorescence microscopy. R18 and CF double-labeled RBCs were bound to the HA-expressing CV-1 cells and the pH was adjusted to pH 5 to trigger fusion between the two cells. The transfer of the red dye (R18) indicates the mixing of lipids and the transfer of the green dye (CF) indicates the mixing of soluble contents between the two cells.

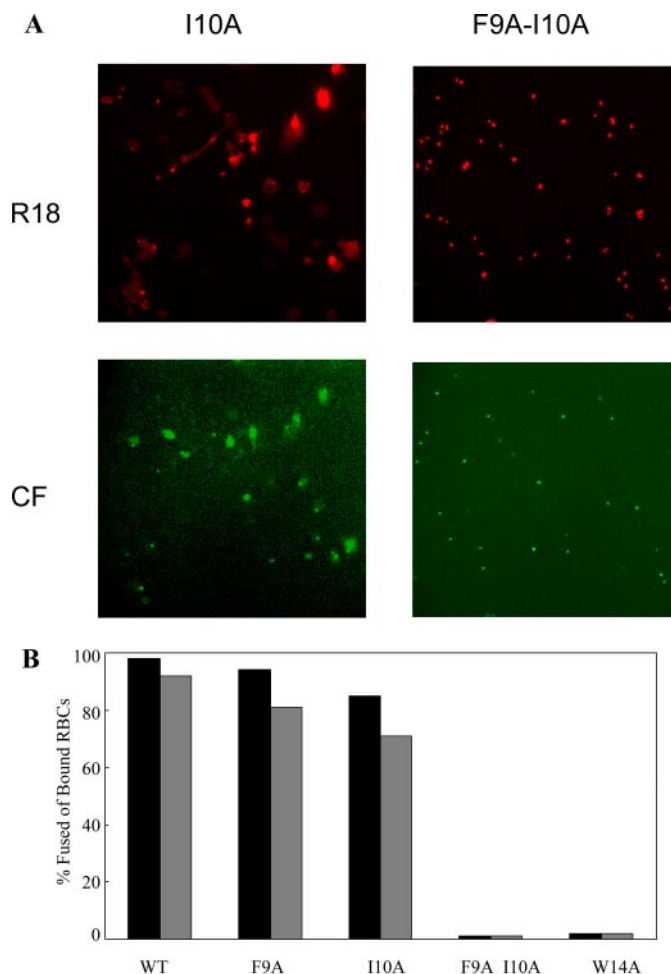


FIGURE 1. Fusion activity of HAs with point mutations I10A and F9A/I10A in the kink region of the fusion domain. R18 and CF double-labeled RBCs were bound to HA-expressing CV-1 cells that were treated with neuraminidase and trypsin. Fusion was triggered by briefly switching the pH to 5. *A*, epifluorescence micrographs of cells that were examined for lipid mixing (*top*) and contents mixing (*bottom*). *B*, % lipid mixing (*black*) and contents mixing (*gray*) of cells expressing wild-type and mutant HAs. The wild-type, F9A, and W14A data are from Ref. 4.

As shown in Fig. 1, the F9A and I10A mutations did not impair lipid or content mixing, but the F9A/I10A and W14A mutations blocked both. The lipid and contents mixing ratio of I10A were around 88 and 75%, respectively, which are a little lower than those of WT, but similar to those of F9A. Because both dyes are effectively transferred, WT, F9A, and I10A are full fusion phenotypes. However, since neither dye is transferred in the F9A/I10A and W14A mutants, these mutations are identified as non-fusogenic.

The kinetics of lipid mixing were further examined by fluorescence spectroscopy. Fusion between prebound cell couples was monitored by fluorescence dequenching after adjusting the pH to 5 (Fig. 2). The I10A mutant had a relatively high rate of lipid mixing, *i.e.* almost as high as that of WT and F9A. The mutant F9A/I10A, however, had a very low initial rate of lipid mixing, which was even lower than that of W14A. These results obtained in bulk from a large population of cells fully support the results obtained on individual cells by fluorescence microscopy.

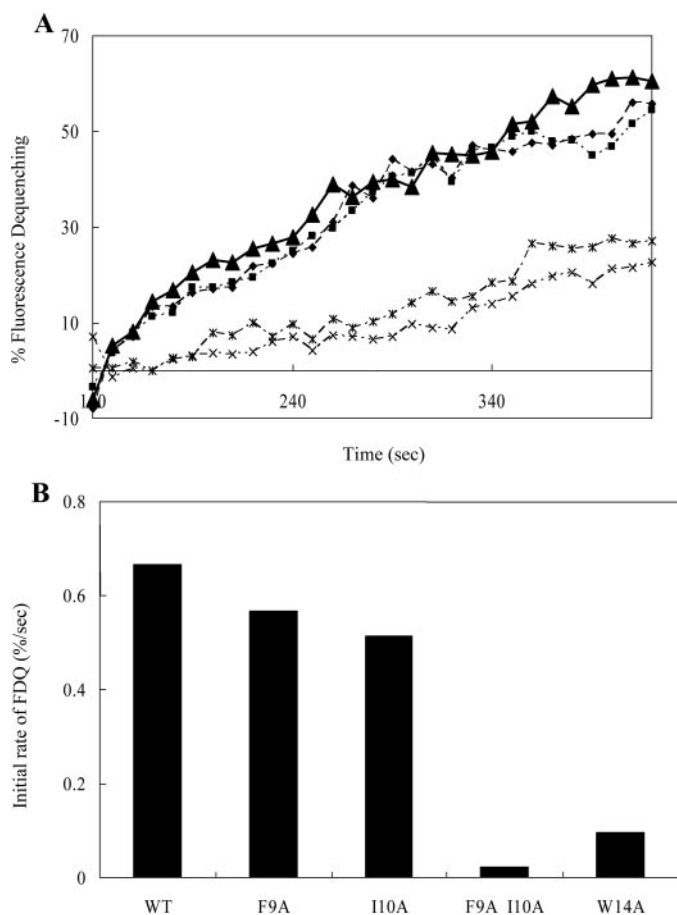


FIGURE 2. Fluorescence dequenching of the lipid probe R18 upon fusion of wild-type and mutant HA-expressing CV-1 cells and labeled RBCs measured by fluorescence spectroscopy. *A*, kinetics of fluorescence. \blacktriangle , wild type; \blacklozenge , F9A; \blacksquare , I10A; $*$, W14A; \times , F9A/I10A. *B*, initial rates of fluorescence dequenching after adjustment of the pH to 5.

Expression and Processing of Mutant HAs on the Cell Surface—To ascertain that these results were not due to expression or proteolytic processing problems, FACS and immunoprecipitation were carried out to examine the level of surface expression and proteolytic processing of HA to form the active heterodimer HA1/HA2. For FACS analysis, the HA-expressing cells were labeled with an anti-HA monoclonal antibody followed by a fluorescein-conjugated secondary antibody. This experiment reveals the percentage of cells that express HA on their surface as well as the HA expression level of the population of surface HA-expressing cells. As shown in Fig. 3, *A* and *B*, the percentage of surface HA-expressing cells and the HA expression level in the HA-expressing cell population were the same for the wild type and the mutants. For immunoprecipitation, transfected CV-1 cells were first treated with a small amount of trypsin followed by labeling of all surface-expressed proteins with sulfo-NHS-LC-biotin. After lysis of the cells, HAs were immunoprecipitated by an anti-HA monoclonal antibody and protein A-conjugated beads. The SDS-polyacrylamide gel of Fig. 3*C* shows that wild type and both mutants were properly cleaved by trypsin into HA1 and HA2. Taken together, these controls show that the observed fusion phenotypes are the results of fusion defects of the mutants, and not the results of deficiencies in surface expression or proteolytic processing.

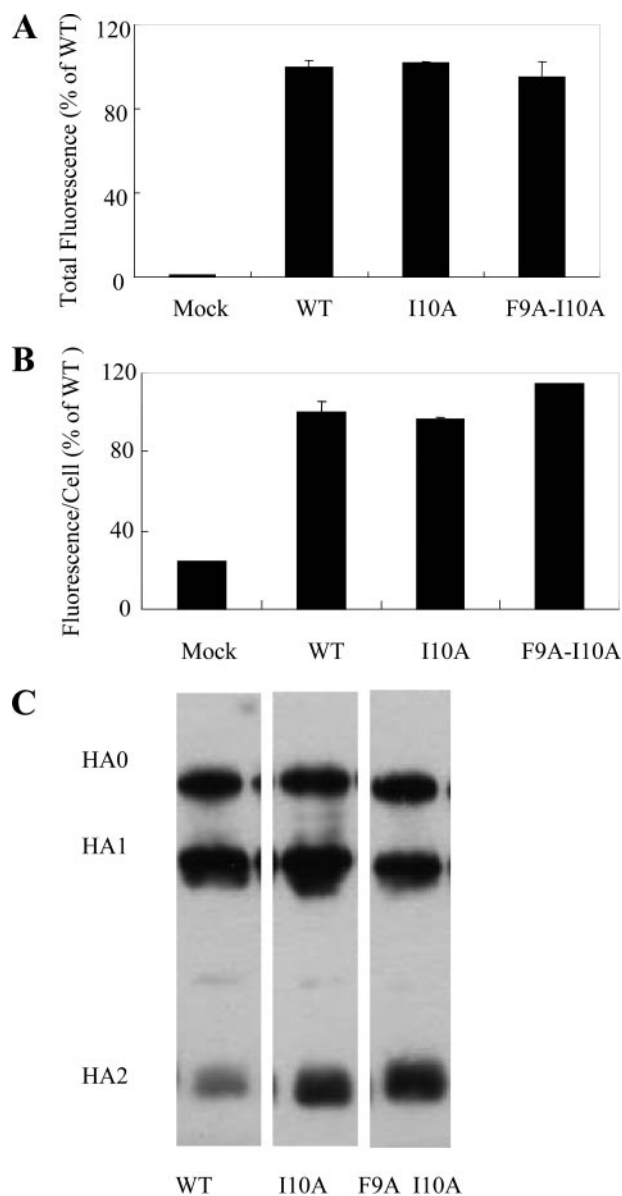


FIGURE 3. Expression and processing of the wild-type and mutant HAs on the surface of CV-1 cells. *A*, FACS analysis of the percent of cells transfected, compared with wild-type HA. *B*, FACS analysis of the fluorescence intensity per cell in the population of transfected cells, compared with wild-type HA. *C*, SDS-polyacrylamide gels of immunoprecipitated HAs showing that wild-type and mutant HAs were cleaved to HA1 and HA2 after treatment with trypsin.

Binding of HA Fusion Domains to Lipid Bilayers—To investigate the strengths of the fusion domain-lipid interactions, we used synthetic fusion peptides comprising the first 20 amino acids of the HA2 wild-type (strain X31) or mutant sequences followed by the non-perturbing hydrophilic solubility tag GCGKKKK (11). We first measured the equilibrium partition coefficients and free energies of the binding of the wild-type and mutant fusion domains to lipid bilayers composed of POPC/POPG (4:1) by isothermal titration calorimetry. Small aliquots of SUVs were injected into the reaction cell containing the soluble fusion domains. Saturating binding curves were obtained as shown for I10A in supplemental Fig. S1*A*. The small residual heats that were produced after saturation are the heats of dilution that were subsequently subtracted using a control

TABLE 1

Thermodynamic parameters of the binding of wild-type and mutant fusion domains to lipid bilayers composed of POPC/POPG (4:1) at pH 5

Mutant	$K_{\text{app}}/10^5$ M^{-1}	$K_0/10^4$ M^{-1}	$\Delta\Delta G$ kcal/mol	$\Delta\Delta H$ kcal/mol	$-T\Delta\Delta S$ kcal/mol
WT ^a	6.3 ± 0.5	1.5 ± 0.1	-7.2 ± 0.4	-15.8 ± 0.5	8.6 ± 0.6
F9A ^a	5.1 ± 0.6	1.2 ± 0.2	-7.0 ± 0.7	-16.4 ± 0.5	9.4 ± 0.9
I10A	5.5 ± 0.8	1.3 ± 0.3	-7.1 ± 0.6	-15.2 ± 0.8	8.1 ± 1.0
F9A/I10A	0.30 ± 0.03	0.073 ± 0.005	-5.4 ± 0.4	-8.2 ± 0.4	2.8 ± 0.6
W14A ^a	0.50 ± 0.04	0.12 ± 0.01	-5.6 ± 0.3	-8.9 ± 0.4	3.3 ± 0.5

^a Data of WT, F9A, and W14A are from Lai *et al.* (4).

experiment. The data were plotted as mol fraction bound peptide/lipid *versus* free peptide, which gives a straight line with a slope corresponding to the apparent partition coefficient K_{app} (supplemental Fig. S1B).

Because the peptides are positively charged and the membranes are negatively charged, the concentration of free peptides near the membrane surface is different from that in buffer far away from the membrane. The contributions of this electrostatic effect, calculated by the Gouy-Chapman theory, were subtracted from K_{app} as previously described (11), resulting in the intrinsic partition coefficients K_0 , and free energy change, $\Delta G = -RT\ln K_0$, describing the non-electrostatic fusion domain interactions with the lipid bilayer. As shown in Table 1, the free energy changes of WT, F9A, and I10A are around -7 kcal/mol, while those of F9A/I10A and W14A are only about -5.5 kcal/mol.

We also measured the enthalpy change associated with the binding of the fusion domains to lipid bilayers. In this case, small aliquots of peptides were injected into the reaction cell containing a large excess of SUVs. Therefore, all peptides bind to lipids at each titration step (supplemental Fig. S1C and S1D). Heats of mixing and the contribution of the binding of the hydrophilic solubility tag are subtracted by a control measurement with the tag peptide Ach7 alone (12), resulting in the values of $\Delta\Delta H$ in Table 1. WT, F9A, and I10A had similar enthalpy changes on the order of -15 to -16 kcal/mol, while the fusion-deficient mutants F9A/I10A and W14A had significantly smaller negative enthalpy changes on the order of -8 to -9 kcal/mol. Using the enthalpy and free energy changes, the entropy changes were calculated from $\Delta G = \Delta H - T\Delta S$ (Table 1). As noted before (12), the fusion domain-lipid interactions are driven by enthalpy and opposed by entropy. The enthalpy change, which includes contributions from folding and lipid insertion, provides the driving force for fusion domain insertion.

Perturbation of Lipid Bilayer Structure by Fusion Domains—We used polarized ATR-FTIR spectroscopy to investigate the perturbation of lipid order by the binding and membrane insertion of the HA fusion domains. The order of the acyl chains in a lipid bilayer is described by the order parameter, S_L , which may be calculated from the experimental ATR dichroic ratio, R^{ATR} , *i.e.* the ratio between the absorptions of parallel and perpendicular polarized infrared light at the lipid methylene stretch vibration frequencies around 2920 cm^{-1} and 2850 cm^{-1} . A high value of R^{ATR} indicates a low order of the lipid acyl chains, and vice versa, a low value indicates high order. We determined the perturbation of the bilayer structure by comparing the dichroic ratios with and without bound fusion domains. The

TABLE 2

ATR dichroic ratios of the lipid methylene stretching vibrations and derived orders parameters in the absence and presence of bound wild-type and mutant fusion domains

	R^{ATR} 2920 cm^{-1}	R^{ATR} 2850 cm^{-1}	S_L
Lipid only	1.36 ± 0.03	1.34 ± 0.03	0.34 ± 0.01
WT ^a	1.16 ± 0.06	1.12 ± 0.05	0.58 ± 0.02
F9A ^a	1.18 ± 0.04	1.17 ± 0.03	0.55 ± 0.01
I10A	1.22 ± 0.04	1.19 ± 0.05	0.50 ± 0.02
F9A/I10A	1.30 ± 0.04	1.27 ± 0.03	0.41 ± 0.01
W14A ^a	1.32 ± 0.05	1.32 ± 0.05	0.38 ± 0.01

^a Data of WT, F9A, and W14A are from Lai *et al.* (4).

results presented in supplemental Fig. S2 and Table 2 show that the fusion-deficient mutants F9A/I10A and W14A perturb the bilayer structure to a significantly smaller degree than the fusion-supporting WT and mutants F9A and I10A. As shown in Fig. 4, these results correlate well with the binding and fusion data. The higher lipid order induced by the fusogenic domains may be related to a dehydration of the membrane surface, which is a prerequisite for membrane fusion. The fusion-deficient mutants do not bind strongly enough and thereby may be unable to sufficiently dehydrate the membrane surface in preparation for fusion. The active fusion domains also reduce the entropy of the system more than the inactive fusion domains when they bind to membranes (Table 1), but it is not clear whether this is primarily an effect of lipid or protein ordering.

NMR Structure of F9A Mutant Fusion Domain in DPC—We previously obtained the structures of the wild-type and W14A fusion domains in DPC micelles by homonuclear NMR spectroscopy (3, 4). We found that the wild type adopted an angled boomerang structure with a fixed kink region while W14A adopted an angled structure with a flexible hinge. In order to consolidate the notion that functional fusion domains require a fixed-angle kink, F9A was selected for structural analysis by NMR spectroscopy. CD spectra of F9A in DPC micelles are similar to those in lipid bilayers composed of POPC and POPG, indicating that the helical secondary structure is similar in the two environments (data not shown).

Homonuclear TOCSY and NOESY spectra of F9A bound to DPC micelles at pH 5 were acquired and fully assigned. The chemical shifts are shown in supplemental Table S1. The HN and H α chemical shifts of the first 8 and the last 5 residues are little changed compared with those of wild type, but relatively large chemical shift differences are seen in the kink region formed by the residues 10–15 (supplemental Fig. S3). This indicates that the conformations of the N-terminal and the C-terminal ends of the two fusion domains are similar. The N- and C-terminal ends of F9A are likely helical because we found

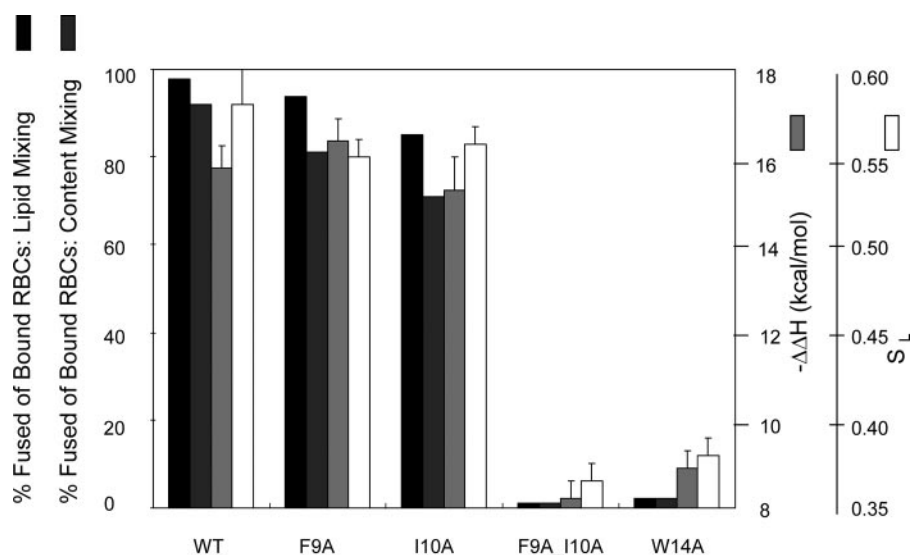


FIGURE 4. Correlation of fusion activity, enthalpy of binding to lipid bilayers, and lipid perturbation (represented by lipid order parameter S_D) of wild-type and mutant HAs and corresponding fusion domains. The data of wild type, F9A, and W14A are from Ref. 4.

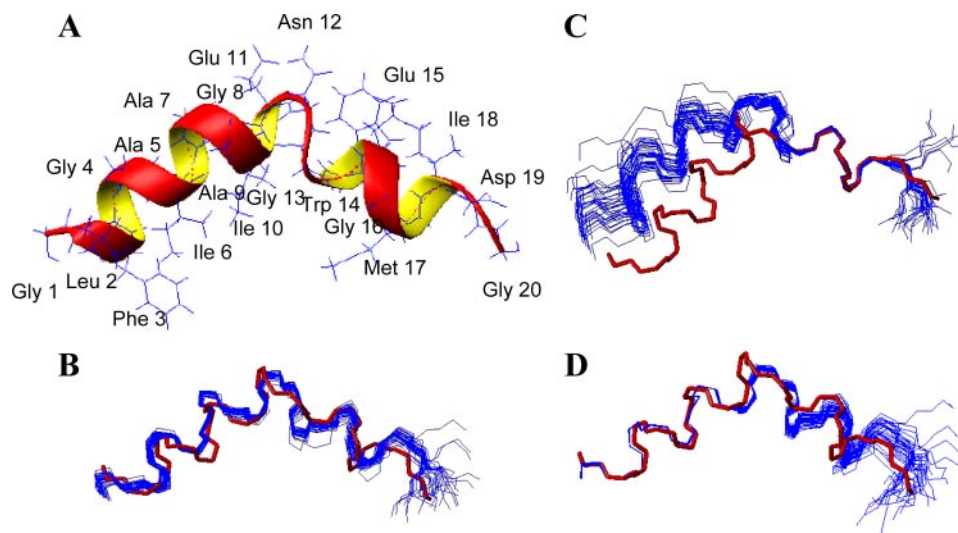


FIGURE 5. NMR structure of the F9A fusion domain in DPC micelles at pH 5. *A*, most representative structure of the F9A fusion domain in DPC micelles at pH 5 with side chains inserted. *B–D*, 35 lowest energy conformers of F9A (blue) superposed with the most representative structure of the wild-type fusion domain (from Ref. 3) at pH 5 (red). *B*, residues 1–20 aligned; *C*, residues 14–18 aligned; *D*, residues 1–11 aligned.

medium-range NOEs [$d_{\alpha N}(i, i+3)$, $d_{\alpha N}(i, i+4)$, and $d_{\alpha\beta}(i, i+3)$] from Leu² to Ala⁹ and from Glu¹⁵ to Asp¹⁹ (data not shown).

The structure of F9A in DPC was calculated from a total of 147 non-redundant upper-limit restraints and 63 dihedral angle restraints that were obtained from the NOE and chemical shift data, respectively. The backbone structures of the 35 lowest energy conformers are shown in Figs. 5, *B–D* and the closest-to-the-mean structure with side chains inserted is shown in Fig. 5*A*. The corresponding structural statistics are presented in supplemental Table S2. All structures are angled and show a kink around Asn¹². The alignment of all backbone atoms (residues 1–20) is quite good (r.m.s.d. 0.79 ± 0.40 Å), indicating that the kink in F9A, like in wild type, has a fixed angle of about 120° (Fig. 5*B*). The alignments from residues 2 to 12 and from 15 to 18 are very good (r.m.s.d. 0.10 ± 0.06 Å and 0.19 ± 0.08 Å,

respectively) as shown in Figs. 5*C* and *D* and Table 2. Like wild type, the N-terminal arm forms an unbroken α -helical structure from residues 2 to 10, and the C-terminal arm forms a short 3_{10} -helix from residues 15 to 18. A turn is formed by residues 10–14, which redirects the polypeptide chain to form the $\sim 120^\circ$ angle. Four hydrogen bonds are observed in all conformers and are thought to stabilize the structure in the kink region. These are the hydrogen bonds between the amide NHs of Asn¹² and Gly¹³ and the carbonyl of Ala⁹, the hydrogen bonds from the amide NH of Trp¹⁴ to the carbonyl of Ile¹⁰, and the amide NH of Asn¹² to the carbonyl of Glu¹⁵. Even though the wild-type and F9A structures are very similar (compare red overlay of wild type on blue ensemble of F9A structures in Fig. 5), there are subtle differences in the kink region. For example, the torsion angle ψ in Asn¹² is different between the two molecules. As a result, the C-terminal helix of F9A is bent $\sim 20^\circ$ away from the plane defined by the axes of the two helices of wild type. Despite this minor difference, the overall similarity between the two structures is quite striking.

EPR Power Saturation Experiments and Docking of F9A NMR Structure into Lipid Bilayer—To obtain information about the insertion depth of the F9A fusion domain in the lipid bilayer, site-directed spin-labeling and power saturation EPR experiments in the presence of

N₂, O₂, and NiEDDA were carried out. Residues 3, 7, 12, and 18 were separately changed to cysteines and labeled with MTSSL. Mutations to cysteines of these residues do not affect the secondary structures of the fusion domains as shown in previous work for wild type (3) and here for F9A (data not shown). As shown in Fig. 6*A*, the spin-label attached to residue 3 inserts deeply into the core of the lipid bilayer, while spin-labels attached to residues 7 and 18 insert shallower, and the spin-label attached to residue 12 is very close to the aqueous layer. The most representative conformer of the NMR structural ensemble was docked into the lipid bilayer using the insertion depths measured by power saturation EPR as distance restraints. As shown in Fig. 6*B*, the C α of Asn¹² locates to about the middle of the interface region and the N- and C-terminal arms of the boomerang structure insert more deeply into the lipid bilayer. The N-terminal arm inserts most deeply into the

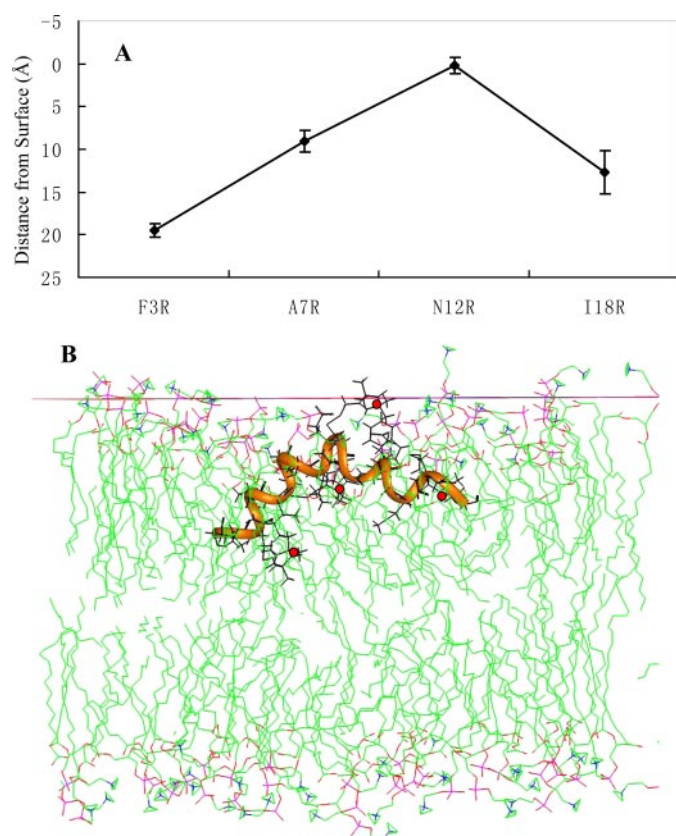


FIGURE 6. A, depths of four side chains (Phe³, Ala⁷, Asn¹², and Ile¹⁸) of the F9A fusion domain in POPC:POPG (4:1) lipid bilayer measured by site-directed spin-labeling and power-saturation EPR spectroscopy. B, F9A fusion domain docked into a POPC lipid bilayer using the distance constraints from EPR spectroscopy and the most representative structure of F9A from NMR spectroscopy. The membrane "surface" (red line) is defined by the average position of the lipid phosphate groups.

core of the bilayer at an angle of about 40° from the membrane plane. Overall, this mode of insertion is very similar to that previously described for the wild-type fusion domain (3).

ERP Line-shape Analysis to Probe Local Environment of Wild-type and Mutant Fusion Domains in Lipid Micelles and Bilayers—The line shapes of EPR spectra are sensitive to motions of spin-labeled proteins, which in turn depend on their local environment. Because our NMR data indicated that the wild-type and F9A fusion domains have fixed-angle and W14A has a flexible-angle boomerang structure in DPC micelles, we analyzed the line shapes of EPR spectra in DPC micelles and POPC:POPG bilayers to examine (i) whether these differences were also manifest in EPR spectra in micelles and (ii) whether the same differences also translated into motional differences in lipid bilayers. The same analysis was also carried out for F9A/I10A, for which no NMR high-resolution structure is currently available. Residues 3 and 18 were individually changed to cysteines and labeled with MTSSL in wild type and each mutant. CD spectra of the native and cysteine-mutated fusion domains bound to lipid bilayers showed minima at 208 and 222 nm in all cases, indicating that the mutations did not significantly affect the helical structures of these fusion domains in lipid bilayers (data not shown).

Normalized EPR spectra of WT, F9A, W14A, and F9A/I10A labeled in positions 3 and 18 in solution, in DPC micelles, in

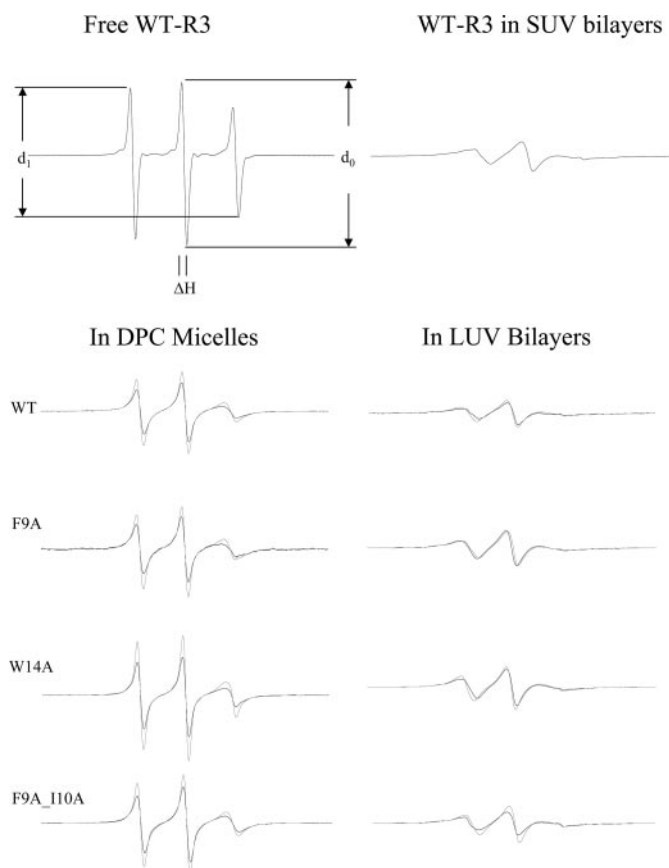


FIGURE 7. EPR spectra normalized to equal areas of wild-type and F9A and W14A mutant fusion domains labeled with MTSSL in solution (top left), DPC micelles (bottom left), and POPC:POPG (4:1) bilayers (right) at pH 5. In each case, the black lines represent the R3 spin labels, and gray lines represent the R18 spin labels. Definitions of line shape parameters, ΔH , d_0 , and d_1 are indicated in the top left spectrum.

TABLE 3

EPR line shape parameters ΔH (line-width) and d_0 (peak-to-peak height) of single-spin-labeled wild-type and mutant fusion domains in micelle and lipid bilayers at pH 5

Mutant	Spin-label positions	DPC		SUV		LUV	
		ΔH	d_0	ΔH	d_0	ΔH	d_0
WT	R3	2.49	0.078	3.71	0.029	3.96	0.029
	R18	2.30	0.11	3.66	0.039	3.81	0.036
F9A	R3	2.39	0.089	3.66	0.046	3.81	0.046
	R18	2.25	0.11	3.70	0.047	3.66	0.046
F9A/I10A	R3	2.49	0.097	3.81	0.041	3.61	0.046
	R18	2.29	0.13	3.47	0.053	3.41	0.050
W14A	R3	2.25	0.10	3.37	0.048	3.60	0.048
	R18	2.05	0.16	3.13	0.054	3.33	0.056

POPC:POPG (4:1) SUVs, and in POPC:POPG (4:1) LUVs are shown in Fig. 7. The EPR line shapes were parameterized by a line width (ΔH) and a peak-to-peak amplitude (d_0) of the central line of the EPR spectrum as indicated at the top left in Fig. 7. These parameters collected for all spectra of Fig. 7 are summarized in Table 3. A reduction of mobility results in broader lines, *i.e.* a larger ΔH , and a smaller d_0 . Inspection of these data indicate that the mobilities decrease depending on environment in the order solution > DPC > SUV \approx LUV for all fusion domains. In a given fusion domain and environment, the mobility of the C-terminal arm (probed at residue 18) is always greater than that of the N-terminal arm (probed at residue 3).

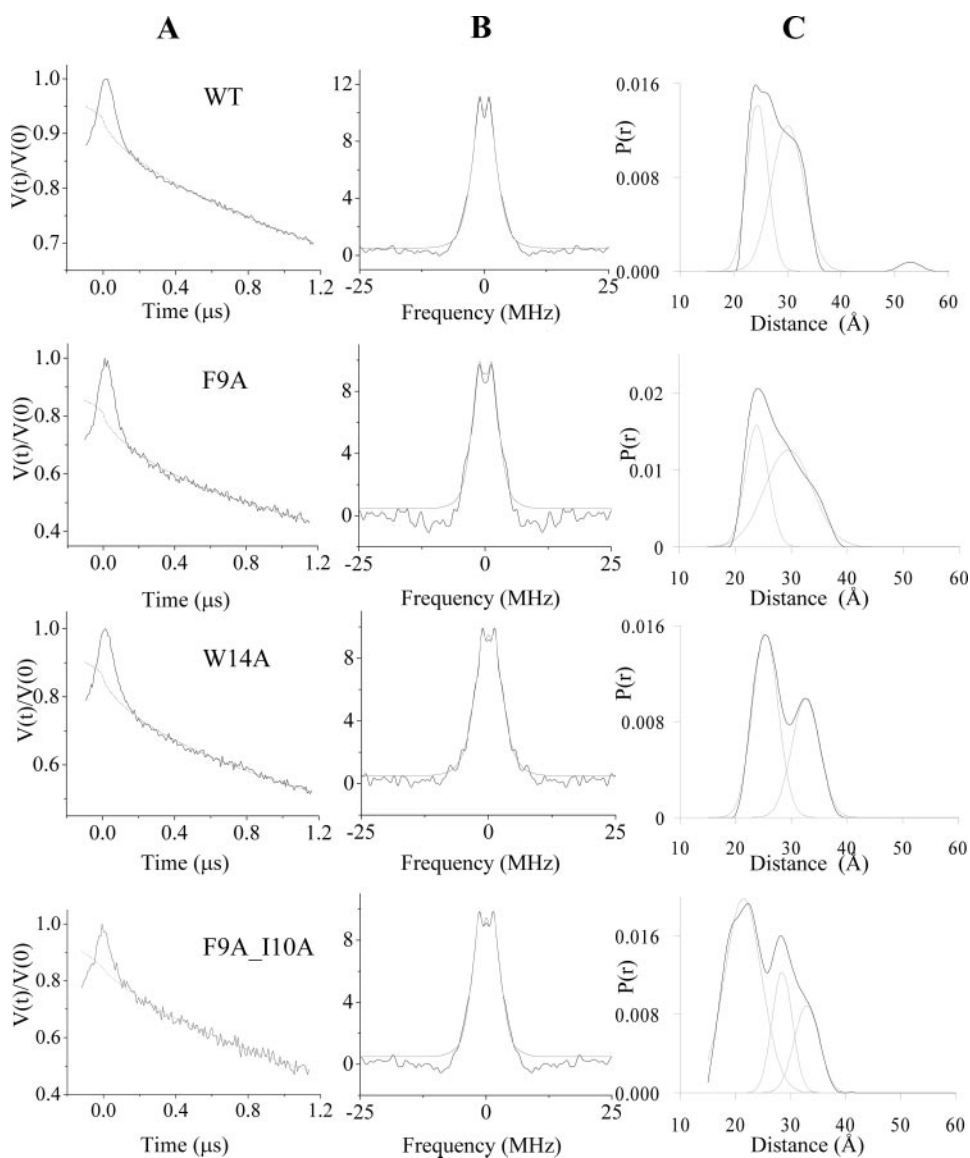


FIGURE 8. DEER spectroscopy to measure distance distributions of the two arms of wild-type, F9A, W14A, and F9A/I10A mutant fusion domains in POPC:POPG (4:1) bilayers at pH 5. *A*, four-pulse DEER time-domain spectra (solid lines) with the background correction (dotted lines). *B*, Pake powder patterns of dipole-dipole couplings obtained after Fourier transformation of background-corrected DEER time evolutions. The noisy lines are the experimental spectra, and the smooth lines are the best fits with the corresponding distance distributions shown in *C*. *C*, best-fit distance distributions between two spins attached to residues R3 and R18 of the corresponding fusion domains. The dashed lines are fits of the experimental distance distributions with a minimal number of Gaussian components in each case. The fit results are summarized in Table 4.

Most interestingly, the mobilities of both positions of W14A and F9A/I10A are always greater than those of the corresponding positions of WT and F9A in DPC micelles and lipid bilayers. Therefore, these results are entirely consistent with the NMR structures in DPC micelles, which showed that W14A is more flexible than WT and F9A. The relative mobilities of the fusion-inactive mutant F9A/I10A are in between those of WT and the other fusion-inactive mutant W14A. Although a high resolution structure of F9A/I10A has not been determined, this domain, therefore, is likely also somewhat flexible like that of W14A, for which an NMR structure is available (4). It is also important to note that the higher mobilities that are observed for both arms of the boomerang of W14A and F9A/I10A compared with WT and F9A are not only seen in detergent micelles

but also in lipid bilayers, which indicates that these structural dynamical differences must at least qualitatively also occur in lipid bilayers, where high resolution structures cannot be obtained by solution NMR.

Flexibility of Kink Region of Wild-type and Mutant Fusion Domains in Lipid Bilayers by DEER and CW EPR Spectroscopy—If W14A and F9A/I10A have more flexible structures in membranes than wild type and F9A, we should be able to measure altered distance distributions between the two arms of the boomerang by measuring the dipolar coupling of two electron spins that are placed on the opposite arms of the structures. To this end, wild-type, F9A, W14A, and F9A/I10A fusion domains were each double-labeled with MTSSL at cysteines in positions 3 and 18. Control CD experiments showed that these cysteine modifications did not appreciably change the secondary structures of any of the four fusion domains in lipid bilayers (data not shown). The dipole-dipole coupling between two electron spins depends on the inverse cube of the distance r between them and is on the order of 25 MHz for two nitroxide spins that are separated by ~ 2 nm. Dipolar couplings of this magnitude can be accurately measured by a four-pulse DEER experiment, which produces a spin echo that is modulated by the frequency of the dipolar interaction (13). DEER time evolution data of the four double-labeled fusion domains bound to lipid bilayers

composed of POPC:POPG(4:1) were collected and normalized to the signal at time 0 as shown in Fig. 8A. Fourier transformation of these time domain data leads to Pake powder patterns, shown in Fig. 8B, for isotropically distributed proteins, such as our vesicle-bound fusion domains. The splitting of the Pake doublet depends on the distance between the two spins that are coupled by dipolar interactions in Equation 1,

$$\omega_{dd} = \frac{2\pi g_1 g_2}{g_e^2} (3\cos^2\theta - 1) \frac{52.04}{r^3} [\text{MHz} \cdot \text{nm}^3], \quad (\text{Eq. 1})$$

where ω_{dd} is the angular frequency of the splitting, g_1 , g_2 , and g_e , are the g values of the two spins and the free electron, respectively, and θ is the angle between the spin-spin vector and the

TABLE 4
Distance distributions between the two arms of the fusion domains bound to lipid bilayers determined by DEER spectroscopy

Mutant	Distance		
	1 st component ^a	2 nd component ^a	3 rd component ^a
	Å (rel. weight %)	Å (rel. weight %)	Å (rel. weight %)
WT	24.4 (43%)		30.0 (57%)
F9A	23.8 (37%)		29.5 (63%)
F9A/I10A	21.4 (61%)	28.5 (21%)	33.0 (18%)
W14A	25.3 (59%)		32.6 (41%)

^a Best fit Gaussian components of the distance distributions in Fig. 8C.

magnetic field (13). For flexible molecules, Pake patterns are better represented by distance distributions rather than single distances. The best fit distance distributions that are fitting the experimental Pake patterns are shown in Fig. 8C.

Wild type and F9A have similar distance distributions with one component centered at 24 Å and the other component centered at 30 Å, although the longer distance component of F9A could potentially be subdivided into two subcomponents (Table 4). The distance distributions of W14A and F9A/I10A are bimodal with components at 25 Å and 33 Å in the case of W14A and three components at 21, 29, and 33 Å in the case of F9A/I10A (Table 4). These component fits represent the simplest possible solutions for easy comparison. Obviously, better fits could be achieved with more components in some cases. The main point of this comparison is that W14A and especially F9A/I10A can assume longer distances and wider distance distributions than wild type and F9A in lipid bilayers. The NMR structure in DPC micelles suggests that W14A has a flexible hinge, with a broad distribution of the kink angles. Therefore, some conformers may be more extended than the others. Thus, the NMR and EPR structural data of W14A in different environments are consistent with each other. The situation of F9A/I10A is likely similar to that of W14A although we do not have high resolution NMR data for this mutant. We conclude that the flexibility of the kink region is most likely an intrinsic property of these structures, irrespective of whether they are bound to lipid micelles or bilayers. This is reassuring because the flexibility observed in the NMR structure of W14A potentially could also have been a result of experimental difficulties to observe a sufficient number of NOEs and bond angle restraints to fix the structure in this region. The results also confirm that DPC micelles are reasonable surrogates of lipid bilayers for structure determinations of fusion domains by solution-state NMR.

Strong dipolar interactions between electron spins can also be measured by CW X-band EPR spectroscopy. In this case, the spectra of the double-labeled proteins are compared with the sum of the spectra of the two single-labeled proteins and the dipolar interaction is estimated from the difference between the two (14). This method yields good distance estimates in the 8–20 Å distance range (15). We also applied this method to all four fusion domains bound to lipid bilayers composed of POPC and POPG. The data are shown in supplemental Fig. S4. The sums of the single-labeled spectra of wild type and F9A were very similar to the double-labeled spectra and the ratios of the low field to the center field transitions d_1/d_0 were <0.4 suggesting that there was little

interaction between the two spins in these two domains, consistent with distances >20 Å. However, W14A and F9A/I10A showed significant differences between the sums of the single-labeled spectra and the double-labeled spectra, indicating components in each of these ensembles that have spin-spin distances <20 Å. Therefore, even though we refrain from a meaningful quantitative analysis of the CW EPR data, the CW EPR and DEER results are in very good qualitative agreement. Although we cannot extract reliable distance information from the CW method, this agreement is important because the CW data are obtained at room temperature in solution, whereas the DEER method requires measurements on frozen samples at 80 K.

DISCUSSION

The aim of this study was to investigate the importance of the boomerang structure of the influenza HA fusion domain and its defining kink region with regard to its ability to mediate membrane fusion. We also wished to determine the forces and lipid interactions that dictate the stability of the kinked structure at the membrane interface. The structure contains two aromatic side chains, Phe⁹ and Trp¹⁴, that point toward each other in the kink region and that face the hydrophobic interior of the lipid membrane (3). Because aromatic side chains are well known to anchor membrane proteins in the membrane interface (16, 17), it was reasonable to hypothesize that Phe⁹ and Trp¹⁴ would also stabilize the active conformation of the HA fusion domain in membranes. However, recent data were not entirely consistent with this hypothesis. Although mutating Trp¹⁴ to Ala aborted the boomerang structure and function of the HA fusion domain, mutating Phe⁹ to Ala had no effect on the function or lipid interactions (4) and, as we now know, had also only very limited effects on the boomerang structure and membrane position of this fusion domain (Figs. 5 and 6). Therefore, additional factors must contribute to the formation of the active boomerang conformation of the HA fusion domain in membranes. Trp contributes -2.0 kcal/mol more energy to the stability of membrane proteins than Ala, but Phe contributes only -1.2 kcal/mol more (17, 18). Because Ile¹⁰ is located right next to Phe⁹ in the hydrophobic pocket of the boomerang structure (3) and because Ile is expected to contribute another -0.5 kcal/mol over Ala (18), we suspected that both Phe⁹ and Ile¹⁰ were needed to stabilize the N-terminal arm of the boomerang structure in the membrane interface. Indeed, eliminating both hydrophobic residues at the same time aborted fusion, whereas each single mutant alone was not sufficient to eliminate contents or lipid mixing (Figs. 1 and 2).

A first confirmation that an angled boomerang structure is required for fusion comes from the NMR solution structure of F9A in DPC micelles at pH 5 (Fig. 5) and its docking into lipid bilayers by site-directed spin-label EPR spectroscopy (Fig. 6). These results are significant because they serve as a positive control for the importance of the kink region; the only other known structure of a fully functional HA fusion domain in membrane environments is that of wild type (3). Indeed, F9A possesses a very similar structure as wild type with a fixed-angle ($\sim 120^\circ$) kink centered at Asn¹², a long α -helical N-terminal arm, and a short 3_{10} -helix in the C-terminal arm. Both struc-

tures dock into membranes with the $C\alpha$ of Asn¹² roughly aligned at the level of the phosphate groups of the lipid bilayer. In marked contrast, W14A possesses a flexible hinge at Asn¹², the N-terminal arm lies along the membrane interface, and the irregular structured C-terminal arm points out of the bilayer into the solution (4).

Several lines of evidence presented in this work show that the well-structured active fusion domains of wild type and F9A are more rigid than the more flexible structures of the inactive W14A and F9A/I10A mutants not only in DPC micelles but also in lipid bilayers. First, EPR line-shape analysis indicates more motion for both arms of W14A and F9A/I10A than for the two corresponding arms of the wild-type and F9A structures (Fig. 7 and Table 3). This property translates directly from DPC micelles to small and to large unilamellar vesicle environments. Second, DEER and CW EPR distance measurements between two spins placed on either arm of the boomerang structures provide direct evidence that the angles between the two arms are more rigid in the functional wild-type and F9A structures than in the fusion-defective W14A and F9A/I10A structures (Fig. 8 and supplemental Fig. S4). In fact, in all instances the distances measured by DEER spectroscopy in lipid bilayers are roughly consistent with the corresponding distances measured by NMR spectroscopy in lipid micelles. This observation supports our assumption and earlier conclusion (3) that DPC micelles, although more dynamic and more curved, provide an environment that mimics the membrane interface quite well where fusion domains adopt structures that are at least very similar if not identical to those in lipid bilayer membranes.

To better understand the consequences of the structural differences between the different fusion domain mutants and to establish a link to their different functions, we measured their affinities for membrane interfaces and examined their potency to perturb the lipid bilayer structures to which they bind. As was observed before for the wild-type fusion domains (12), the binding of the mutant fusion domains to membranes is dominated by enthalpy and opposed by entropy (Table 1). The active fusion domains bind with about 7–8 kcal/mol more energy to lipid bilayers. This is quite significant and, as the comparison of the bilayer docking results of wild type and F9A on one hand with W14A on the other hand shows, is likely a consequence of the deeper insertion of the functional boomerang structures into membranes compared with the looser surface associations of the more flexible fusion-defective W14A and F9A/I10A mutant structures. The structured active fusion domains that penetrate more deeply also order the lipids more than the inactive flexible fusion domains (Table 2). In fact, the inactive fusion domains have almost no effect on lipid ordering. A more highly ordered system is also evident from the larger decrease in entropy that is observed when active fusion domains bind (Table 1). However, it is not clear what fraction of this change can be attributed to lipid, protein, and water ordering, respectively. We believe that active fusion domains displace waters from the interface or alter the water structure between membranes that are about to fuse, which is a required step to overcome hydration repulsion between membranes prior to forming any fusion intermediate (19).

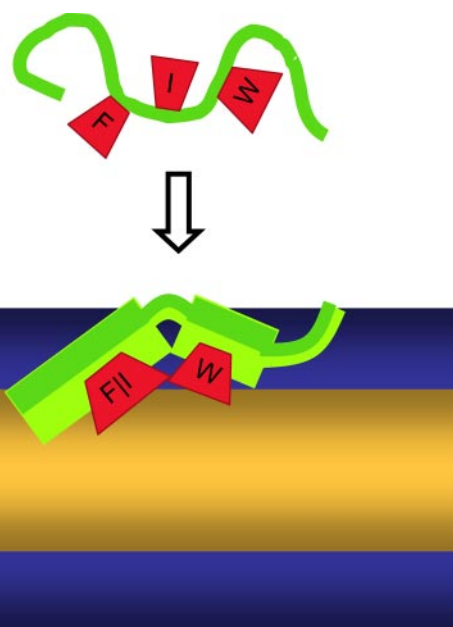


FIGURE 9. **Model of folding and insertion of the influenza HA fusion domain into lipid bilayer.** Two anchoring hydrophobic/aromatic patches composed of Phe⁹ and Ile¹⁰ on one side and Trp¹⁴ on the other side of the kink at Asn¹² are needed to properly fold and lodge the fusion domain in a stable fusion-active boomerang conformation in the membrane interface. Disrupting either one of these anchors leads to flexible interfacial helical conformations that are unable to support fusion.

In summary, there is an excellent correlation between structure, dynamics, membrane penetration, binding strength, lipid perturbation, and membrane fusion of the various fusion domain mutants (Fig. 4). The collective results from this and our earlier studies suggests a model for the interaction of the HA fusion domain with membranes as depicted in Fig. 9. The boomerang structure is clearly stabilized by two hydrophobic clusters consisting of Phe⁹ and Ile¹⁰ on the N-terminal side and Trp¹⁴ on the C-terminal side of the kink. Both are necessary and sufficient to anchor the fusion domain in the proper conformation in the interface of the lipid bilayer. What goes on from this point on to push the two membranes into a fusion configuration is less clear. It may be that the aforementioned replacement of water molecules from the membrane surfaces is sufficient to induce some kind of disorganized lipid stalk between the two membranes that are about to fuse (20). However, what is clear is that the boomerang structure in the interface, that has now been demonstrated to be required for fusion, is incompatible with inducing curvature in the membrane that has frequently been invoked to explain fusion intermediates (21). The boomerang structure in the interface curves membranes in the wrong direction to support an hour glass-type lipid stalk. Fusion protein-induced stalks are probably much more disorganized and stochastic than those that can be observed in pure lipid systems, for example by x-ray diffraction (22). Future experiments are required to address these interesting questions.

Structure Deposition—The F9A structure coordinates have been deposited in the Protein Data Bank (accession code: 2JRD).

Acknowledgments—We thank Dr. Judy White for advice with the cell fusion experiments, Drs. David Cafiso, Steve Lukasik, and Meyeon Kim for help with the DEER experiments and analysis, and Drs. Jeff Ellena and Tomasz Cierpicki for help with collection of NMR spectra.

REFERENCES

1. Tatulian, S. A., Hinterdorfer, P., Baber, G., and Tamm, L. K. (1995) *EMBO J.* **14**, 5514–5523
2. Tamm, L. K. (2003) *Biochim. Biophys. Acta* **1614**, 14–23
3. Han, X., Bushweller, J. H., Cafiso, D. S., and Tamm, L. K. (2001) *Nat. Struct. Biol.* **8**, 715–720
4. Lai, A. L., Park, H., White, J. M., and Tamm, L. K. (2006) *J. Biol. Chem.* **281**, 5760–5770
5. Armstrong, R. T., Kushnir, A. S., and White, J. M. (2000) *J. Cell. Biol.* **151**, 425–437
6. Tamm, L. K., and Tatulian, S. A. (1997) *Q. Rev. Biophys.* **30**, 365–429
7. Delaglio, F., Grzesiek, S., Vuister, G. W., Zhu, G., Pfeifer, J., and Bax, A. (1995) *J. Biomol. NMR* **6**, 277–293
8. Luginbühl, P., Güntert, P., Billeter, M., and Wüthrich, K. (1996) *J. Biomol. NMR* **8**, 136–146
9. Koradi, R., Billeter, M., and Wüthrich, K. (1996) *J. Mol. Graph* **14**, 51–55, 29–32
10. Pannier, M., Veit, S., Godt, A., Jeschke, G., and Spiess, H. W. (2000) *J. Magn. Reson.* **142**, 331–340
11. Han, X., and Tamm, L. K. (2000) *Proc. Natl. Acad. Sci. U. S. A.* **97**, 13097–13102
12. Li, Y., Han, X., and Tamm, L. K. (2003) *Biochemistry* **42**, 7245–7251
13. Jeschke, G. (2002) *Chemphyschem* **3**, 927–932
14. Rabenstein, M. D., and Shin, Y. K. (1995) *Proc. Natl. Acad. Sci. U. S. A.* **92**, 8239–8243
15. Altenbach, C., Oh, K. J., Trabanino, R. J., Hideg, K., and Hubbell, W. L. (2001) *Biochemistry* **40**, 15471–15482
16. Killian, J. A., and von Heijne, G. (2000) *Trends Biochem. Sci.* **25**, 429–434
17. Hong, H., Park, S., Flores-Jiménez, R. H., Rinehart, D., and Tamm, L. K. (2007) *J. Am. Chem. Soc.* **129**, 8320–8327
18. Wimley, W. C., and White, S. H. (1996) *Nat. Struct. Biol.* **3**, 842–848
19. Helm, C. A., Israelachvili, J. N., and McGuiggan, P. M. (1989) *Science* **246**, 919–922
20. Lai, A. L., Li, Y., Tamm, L. K. (2005) in *Interplay of Protein and Lipids in Virus Entry by Membrane Fusion, Protein-Lipid Interactions* (Tamm, L. K., ed) pp. 279–303, Wiley-VCH, Weinheim, Germany
21. Chernomordik, L. V., and Kozlov, M. M. (2003) *Annu. Rev. Biochem.* **72**, 175–207
22. Yang, L., Ding, L., and Huang, H. W. (2003) *Biochemistry* **42**, 6631–6635